ARMY RESEARCH LABORATORY

Mesoscale Modeling of Dynamic Compression of Boron Carbide Polycrystals

by J. D. Clayton

ARL-RP-440 **May 2013**

A reprint from *Mechanics Research Communications*, Vol. 49, pp 57–64.

NOTICES

Disclaimers

The findings in this report are not to be construed as an official Department of the Army position unless so designated by other authorized documents.

Citation of manufacturer's or trade names does not constitute an official endorsement or approval of the use thereof.

Destroy this report when it is no longer needed. Do not return it to the originator.

Army Research Laboratory
Aberdeen Proving Ground, MD 21005-5069

ARL-RP-440 **May 2013**

Mesoscale Modeling of Dynamic Compression of Boron Carbide Polycrystals

J. D. Clayton
Weapons and Materials Research Directorate, ARL

A reprint from *Mechanics Research Communications*, Vol. 49, pp 57–64.

REPORT DOCUMENTATION PAGE

Form Approved
OMB No. 0704-0188

1. REPORT DATE *(DD-MM-YYYY)*	2. REPORT TYPE	3. DATES COVERED (From - To)
May 2013	Reprint	June 2012–March 2013

4. TITLE AND SUBTITLE
Mesoscale Modeling of Dynamic Compression of Boron Carbide Polycrystals

5a. CONTRACT NUMBER

5b. GRANT NUMBER

5c. PROGRAM ELEMENT NUMBER

6. AUTHOR(S)
J. D. Clayton

5d. PROJECT NUMBER
AH80

5e. TASK NUMBER

5f. WORK UNIT NUMBER

7. PERFORMING ORGANIZATION NAME(S) AND ADDRESS(ES)
U.S. Army Research Laboratory
ATTN: RDRL-WMP-C
Aberdeen Proving Ground, MD 21005-5069

8. PERFORMING ORGANIZATION REPORT NUMBER
ARL-RP-440

9. SPONSORING/MONITORING AGENCY NAME(S) AND ADDRESS(ES)

10. SPONSOR/MONITOR'S ACRONYM(S)

11. SPONSOR/MONITOR'S REPORT NUMBER(S)

12. DISTRIBUTION/AVAILABILITY STATEMENT
Approved for public release; distribution is unlimited.

13. SUPPLEMENTARY NOTES
A reprint from *Mechanics Research Communications*, Vol. 49, pp 57–64.

14. ABSTRACT
An anisotropic nonlinear elastic model is advanced for crystals belonging to either of two polytypes of boron carbide ceramic. Crystals undergo transformation to an isotropic, amorphous phase upon attainment of a local state-based criterion associated with a loss of intrinsic stability. The model is implemented using the dynamic finite element method, and is demonstrated on a representative volume consisting of fifty polyhedral grains subjected to uniaxial strain at a uniform high strain rate and shock compression at axial pressures ranging from 10 to 50 GPa. Predicted stress–strain behavior is in close agreement with experimental data. For polycrystals consisting of both polytypes, amorphization initiates at stress levels slightly below the experimental Hugoniot elastic limit, and occurs more readily than observed in experiment. For polycrystals consisting only of the CBC (polar) polytype, amorphization initiates at impact pressures similar to those suggested by experiment. In either case, transformation is promoted by dynamic stress interactions and elastic coefficient mismatch among anisotropic crystals. Results support a previous conjecture that amorphization is related to shear instability and cross-linking of the CBC chain.
in the polar polytype.

15. SUBJECT TERMS
ceramic, elasticity, boron carbide, shock compression, numerical simulation

16. SECURITY CLASSIFICATION OF:			17. LIMITATION OF ABSTRACT	18. NUMBER OF PAGES	19a. NAME OF RESPONSIBLE PERSON
a. REPORT	b. ABSTRACT	c. THIS PAGE			J. D. Clayton
Unclassified	Unclassified	Unclassified	UU	14	19b. TELEPHONE NUMBER (*Include area code*) 410-278-6146

Mechanics Research Communications 49 (2013) 57–64

Contents lists available at SciVerse ScienceDirect

Mechanics Research Communications

journal homepage: www.elsevier.com/locate/mechrescom

Mesoscale modeling of dynamic compression of boron carbide polycrystals

J.D. Clayton*

Impact Physics, RDRL-WMP-C, US Army Research Laboratory, Aberdeen Proving Ground, MD 21005-5066, USA

ARTICLE INFO

Article history:
Received 14 September 2012
Received in revised form 3 December 2012
Available online xxx

Keywords:
Finite strain
Intrinsic stability
Shock compression
Ceramic crystal
Numerical simulation

ABSTRACT

An anisotropic nonlinear elastic model is advanced for crystals belonging to either of two polytypes of boron carbide ceramic. Crystals undergo transformation to an isotropic, amorphous phase upon attainment of a local state-based criterion associated with a loss of intrinsic stability. The model is implemented using the dynamic finite element method, and is demonstrated on a representative volume consisting of fifty polyhedral grains subjected to uniaxial strain at a uniform high strain rate and shock compression at axial pressures ranging from 10 to 50 GPa. Predicted stress–strain behavior is in close agreement with experimental data. For polycrystals consisting of both polytypes, amorphization initiates at stress levels slightly below the experimental Hugoniot elastic limit, and occurs more readily than observed in experiment. For polycrystals consisting only of the CBC (polar) polytype, amorphization initiates at impact pressures similar to those suggested by experiment. In either case, transformation is promoted by dynamic stress interactions and elastic coefficient mismatch among anisotropic crystals. Results support a previous conjecture that amorphization is related to shear instability and cross-linking of the CBC chain in the polar polytype.

Published by Elsevier Ltd.

1. Introduction

As a result of their high hardness, high stiffness, and relatively low mass density, ceramic materials are used frequently in industrial and military applications. Examples of the latter include ballistic protection systems, i.e., armor, for vehicular and personal protection.

A ceramic material of high current interest is boron carbide, B_4C. Single crystals of boron carbide exhibit a rhombohedral (i.e., trigonal) crystal structure: space group $R\bar{3}m$, centrosymmetric point group $\bar{3}m$, and Laue group RI. Various polytypes (i.e., structural variants) exist. In the boron carbide unit cell, C–C–C or C–B–C atomic chains are aligned with the [0 0 0 1] direction (hexagonal notation) and thread the basal layers of icosahedra located at the rhombohedral vertices (Yan et al., 2009). Strictly, the rhombohedral space group description applies for the particular polytype with ideal structure B_{12}(CCC), denoted herein simply as "CCC". Slight distortion from a trigonal structure may occur in other polytypes. The polar CBC polytype, with structure formula $B_{11}C_p$(CBC) and denoted herein simply as "polar", is most thermodynamically stable (i.e., lowest ground state energy) and thought most abundant (Fanchini et al., 2006); stoichiometry of boron carbide may also depart from the ideal boron-to-carbon ratio of B_4C, with lower carbon content possible (Dodd et al., 2002).

Polycrystalline boron carbide, with grains of typical sizes on the order of 10 μm, has a low density of 2.52 g/cm^3, high elastic modulus of 470 GPa (McClellan et al., 2001), high hardness on the order of 30 GPa, and a large Hugoniot elastic limit (HEL) on the order of 15–20 GPa (Vogler et al., 2004; Zhang et al., 2006). Ductility of boron carbide is low; though partial dislocations, stacking faults, and twins have been observed, such defects are thought to be relatively scarce and/or immobile during high rate deformation in commercial material produced by hot pressing. Instead, under impact loading, strength and stiffness of the material are thought to be limited by amorphization and cleavage fracture (Chen et al., 2003). Shock-induced amorphization of boron carbide was discovered during post-mortem examination of fragments recovered from ballistic experiments (Chen et al., 2003), where it was suggested that onset of amorphization may be associated with loss of intrinsic stability in the sense of Born (1940). Previously, association of the Born instability with amorphization was posited for quartz (Gregoryanz et al., 2000), which like boron carbide, has a rhombohedral crystal structure and demonstrates a decrease in elastic shear stiffness $\mathbf{C}_{44}$ at high pressure.

Density Functional Theory (DFT) calculations of hydrostatic loading (Fanchini et al., 2006) predicted collapse of the crystal structure of boron carbide into amorphous regions consisting of a mixture of carbon and boron icosahedra, with segregation most energetically favorable for the CCC polytype. First principles calculations (Yan et al., 2009) implied that amorphization follows cross-linking of the C–B–C atomic chain of the boron carbide unit cell with icosahedral atom(s) at a vertex of the rhombohedral unit

* Tel.: +1 4102786146.
E-mail address: john.d.clayton1.civ@mail.mil

0093-6413/$ – see front matter. Published by Elsevier Ltd.
http://dx.doi.org/10.1016/j.mechrescom.2013.02.005

cell in the polar polytype. The cross-linked structure is unstable at ambient pressure; hence, amorphization and fracture may occur on decompression. Cross-linking occurred for uniaxial straining along the c-axis ([0 0 0 1]-direction) at an axial pressure around 20 GPa but was not observed for hydrostatic compression to 60 GPa. Amorphization has also been observed in dynamic indentation (Subhash et al., 2008). Recent DFT results (Taylor et al., 2011) report variations of elastic stiffness components of several polytypes of boron carbide with increasing hydrostatic pressure. A decreasing tangent elastic coefficient $\mathbf{C}_{44}$ with increasing pressure was predicted, leading to a vanishing eigenvalue of 6×6 stiffness matrix $\mathbf{C}$ at hydrostatic pressure $p\approx 44$ GPa in the CCC polytype and $p\approx 68$ GPa in the polar polytype. These vanishing eigenvalues correspond to onset of the aforementioned Born instability.

In previous work (Clayton, 2012), a third-order anisotropic, nonlinear elastic continuum model was developed for CCC and polar CBC polytypes of boron carbide single crystals, using a combination of published data from experiments and first principles (Lee et al., 1992; McClellan et al., 2001; Yan et al., 2009; Taylor et al., 2011). This model was used to predict the onset of mechanical instability, according to several intrinsic criteria (Hill, 1975; Parry, 1978, 1980a; Milstein and Hill, 1979; Wang et al., 1995; Morris and Krenn, 2000), in single and polycrystals deformed homogeneously and elasto-statically. It was determined that the particular intrinsic "B-criterion" corresponding to incremental loading by the Cauchy stress predicted the earliest onset of instability and correlated with the experimental HEL for uniaxial-strained polycrystals (Clayton, 2012). As discussed in Appendix A, in contrast to classical elastic stability criteria that depend on the load environment and may require consideration of global inequalities (Ogden, 1984), "intrinsic" or "internal" stability criteria (Parry, 1978, 1980a; Morris and Krenn, 2000; Clayton and Bliss, unpublished) depend only on the local state (tangent stiffness and local stress). For homogeneous stress fields, intrinsic stability may be sufficient for classical stability if conjugate stress-deformation measures of the classical and intrinsic criteria coincide.

In this paper, the elasticity model of Clayton (2012) is extended to explicitly account for the amorphous phase. In Section 2, a general finite strain framework is first developed in the context of continuum thermomechanics and is then specialized to boron carbide. Amorphization is modeled to occur upon attainment of intrinsic instability. Discussed in Section 3 are model implementation in a dynamic finite element (FE) context and "mesoscale" simulations of shock and dynamic uniaxial compression of B_4C polycrystals. Conclusions follow in Section 4.

2. Theory

A general continuum constitutive theory is developed for solids undergoing a crystal-to-amorphous transformation in Section 2.1. This theory is specialized to boron carbide in Section 2.2.

2.1. Kinematics and thermodynamics

Let $\boldsymbol{x}$ denote the spatial position of a material particle with reference location $\boldsymbol{X}$. Let $\boldsymbol{x}=\boldsymbol{\chi}(\boldsymbol{X},\ t)$ denote the one-to-one motion, with t time. Letting ∇ denote the material gradient, deformation gradient $\boldsymbol{F}$ is

$$\boldsymbol{F}=\nabla\boldsymbol{\chi}=\boldsymbol{F}^{E}\boldsymbol{F}^{\zeta}, \tag{2.1}$$

where $\boldsymbol{F}^{\zeta}$ accounts for deformation due to transformation/amorphization and $\boldsymbol{F}^{E}$ is the remaining elastic deformation associated with local stress and any rigid body rotation. Let $\zeta\in[0,1]$ denote an order parameter distinguishing between crystalline and amorphous phases, and let $\boldsymbol{F}^{\zeta}$ depend locally only on this parameter:

$$\zeta(\boldsymbol{X},t)=0\forall\boldsymbol{X}\in\text{crystal},\quad \zeta(\boldsymbol{X},t)=1\forall\boldsymbol{X}\in\text{amorphous};$$
$$\boldsymbol{F}^{\zeta}=\boldsymbol{F}^{\zeta}[\zeta(\boldsymbol{X},t)],\quad \boldsymbol{F}^{\zeta}(0)=\mathbf{1}; \tag{2.2}$$

with $\mathbf{1}$ the unit tensor. Helmoltz free energy per unit reference volume Ψ is of the functional form

$$\Psi=\Psi[\boldsymbol{E}(\boldsymbol{F}^{E}),\theta,\zeta]. \tag{2.3}$$

Temperature is θ; Green elastic strain is $\boldsymbol{E}=(1/2)(\ \boldsymbol{F}^{E\mathrm{T}}\ \boldsymbol{F}^{E}-\mathbf{1})$. Dependence on $\boldsymbol{X}$ is implicit in (2.3) for a heterogeneous polycrystal whose elastic moduli vary from grain to grain. Interfacial energy associated with phase boundaries is omitted in this description that treats ζ as an internal state variable; such surface energy could be included by extending (2.3) to include dependence on $\nabla\zeta$, as in phase field theory (Clayton and Knap, 2011a).

Let $\boldsymbol{\sigma}$, $\boldsymbol{P}$, and $\boldsymbol{S}$ denote Cauchy, first Piola–Kirchhoff, and second-Piola–Kirchhoff stresses, related by $\boldsymbol{\sigma}=J^{-1}\boldsymbol{P}\boldsymbol{F}^{\mathrm{T}}=J^{-1}\boldsymbol{F}\boldsymbol{S}\boldsymbol{F}^{\mathrm{T}}$ with $J=\det\boldsymbol{F}$. Let $\boldsymbol{v}=\dot{\boldsymbol{\chi}}$ denote particle velocity, $\nabla\boldsymbol{v}=\dot{\boldsymbol{F}}$, and $U=\Psi+\theta\eta$ be internal energy with η entropy per unit reference volume. Let ρ_0 and ρ denote reference and spatial mass densities, and $\boldsymbol{Q}$ the referential heat flux vector. The usual balance laws of continuum field theory (Clayton, 2011a) apply, expressed here in the absence of body forces and heat sources other than conduction:

$$\rho_0=\rho J,\quad \nabla\cdot\boldsymbol{P}=\rho_0\dot{\boldsymbol{v}},\quad \boldsymbol{F}\boldsymbol{P}^{\mathrm{T}}=\boldsymbol{P}\boldsymbol{F}^{\mathrm{T}},\quad \dot{U}=\boldsymbol{P}:\dot{\boldsymbol{F}}-\nabla\cdot\boldsymbol{Q}. \tag{2.4}$$

The Clausius–Duhem inequality can be written

$$\boldsymbol{P}:\dot{\boldsymbol{F}}-\dot{\Psi}-\dot{\theta}\eta-\theta^{-1}\boldsymbol{Q}\cdot\nabla\theta\geq 0. \tag{2.5}$$

Use of (2.1)–(2.4) in (2.5) and applying standard thermodynamic arguments (Clayton, 2011a) results in the hyperelastic stress–strain law, the entropy relation, and a dissipation inequality:

$$\boldsymbol{P}=\frac{\partial\Psi}{\partial\boldsymbol{F}^{E}}\boldsymbol{F}^{\zeta-\mathrm{T}}=\boldsymbol{F}^{E}\frac{\partial\Psi}{\partial\boldsymbol{E}}\boldsymbol{F}^{\zeta-\mathrm{T}},$$
$$\eta=-\frac{\partial\Psi}{\partial\theta},\quad \left[(\boldsymbol{F}^{E\mathrm{T}}\boldsymbol{P}):\frac{\partial\boldsymbol{F}^{\zeta}}{\partial\zeta}-\frac{\partial\Psi}{\partial\zeta}\right]\dot{\zeta}-\frac{1}{\theta}\boldsymbol{Q}\cdot\nabla\theta\geq 0. \tag{2.6}$$

The quantity in square braces can be viewed as a thermodynamic driving force for transformation.

Let a superscript 0 enclosed in parentheses signify a quantity for a pure crystalline phase ($\zeta=0$) and let a superscript 1 signify a quantity for the completely amorphized phase ($\zeta=1$). Free energies of crystal and amorphous phases can be expanded as Taylor series about a reference state wherein $(\boldsymbol{E},\theta)=(\mathbf{0},\theta_0)$:

$$\Psi^{(0)}=\Psi(\boldsymbol{E},\theta,0)=\Psi_0^{(0)}+\frac{1}{2!}\mathbf{C}^{(0)}_{IJKL}E_{IJ}E_{KL}$$
$$+\frac{1}{3!}\mathbf{C}^{(0)}_{IJKLMN}E_{IJ}E_{KL}E_{MN}+\cdots+\Xi^{(0)}(\boldsymbol{E},\theta), \tag{2.7}$$

$$\Psi^{(1)}=J^{\zeta-1}\Psi(\boldsymbol{E},\theta,1)=\Psi_0^{(1)}$$
$$+\frac{1}{2!}\mathbf{C}^{(1)}_{IJKL}E_{IJ}E_{KL}+\frac{1}{3!}\mathbf{C}^{(1)}_{IJKLMN}E_{IJ}E_{KL}E_{MN}+\cdots+\Xi^{(1)}(\boldsymbol{E},\theta). \tag{2.8}$$

Ground state energy of each phase (elastically unstrained and measured at θ_0) is Ψ_0. Isothermal second- and third-order elastic constants (measured at θ_0) are $\mathbf{C}_{IJKL}$ and $\mathbf{C}_{IJKLMN}$. Functions Ξ account for specific heat and thermal expansion in each phase and vanish at $\theta=\theta_0$. Energy is divided by $J^{\zeta}=\det\boldsymbol{F}^{\zeta}$ in (2.8) so that material coefficients are defined per unit unstressed volume of the amorphous phase.

Table 1
Independent nonzero second- and third-order elastic constants for B_4C single crystals (GPa).

Constant	Polar polytype	CCC polytype	Reference
$\mathbf{C}_{11}$	554	487	Taylor et al. (2011)
$\mathbf{C}_{12}$	121	117	Taylor et al. (2011)
$\mathbf{C}_{13}$	65	66	Taylor et al. (2011)
$\mathbf{C}_{33}$	526	525	Taylor et al. (2011)
$\mathbf{C}_{44}$	155	133	Taylor et al. (2011)
$\mathbf{C}_{14}$	−18	−18	Lee et al. (1992)
K_0	236	222	Clayton (2012)
$\mathbf{C}_{111}$	−873	−667	Clayton (2012)
$\mathbf{C}_{112}$	−1668	−1400	Clayton (2012)
$\mathbf{C}_{113}$	−974	−753	Clayton (2012)
$\mathbf{C}_{123}$	−3605	−3913	Clayton (2012)
$\mathbf{C}_{133}$	−873	−667	Clayton (2012)
$\mathbf{C}_{222}$	−873	−667	Clayton (2012)
$\mathbf{C}_{333}$	−873	−667	Clayton (2012)
$\mathbf{C}_{344}$	1645	3015	Clayton (2012)

2.2. Model and parameters for boron carbide phases

For the crystalline phase ($\zeta = 0$), the third-order anisotropic elastic model of Clayton (2012) is implemented. Polar (CBC) and CCC polytypes are considered with rhombohedral symmetry. Second- and third-order elastic constants in the undeformed state – $\mathbf{C}_{\alpha\beta}$ and $\mathbf{C}_{\alpha\beta\gamma}$ in Voigt notation – are listed in Table 1, along with bulk modulus K_0. In calculations that follow in Section 3, temperature effects on the mechanical response of the material are ignored, corresponding to Ξ = constant in (2.7) and (2.8); θ is neither explicitly prescribed nor calculated.

Stress-induced amorphization in B_4C is not well understood, and associated physical properties are not fully known. A number of amorphous structures have been reported from DFT (Fanchini et al., 2006; Ivanshchenko et al., 2009; Yan et al., 2009) with disordered arrangements featuring various atomic clusters, layers, and different coordination among C atoms. Following Ivanshchenko et al. (2009), here it is assumed that amorphous and crystalline phases have the same mass density $\rho_0 = 2.52$ g/cm^3, and that the bulk modulus of the glassy phase $K_1 = 0.96K_0$, as listed in Table 2. Regarding the former assumption (which implies $J^\zeta = 1$), other DFT work (Yan et al., 2009) suggests that mass density may increase on structure collapse, but this possibility is omitted here. In the absence of further data, it is assumed that $\boldsymbol{F}^\zeta = \mathbf{1}$, and that the amorphous phase behaves as an isotropic St. Venant–Kirchhoff solid obeying Cauchy's symmetry relations (Clayton, 2011a) leading to Poisson ratio $\nu = 1/4$ and shear modulus $\mu = (3/5)\mathbf{K}_1$. The isotropic assumption is valid for amorphous solids; Cauchy symmetry, while unproven for this material, corresponds to pairwise central force interactions among atoms and is characteristic of ideal amorphous/glassy materials (Pineda, 2006).

With these model assumptions applied to boron carbide, free energies (2.7) and (2.8) become

$$\Psi^{(0)} = \Psi_0^{(0)} + \frac{1}{2}\mathbf{C}_{\alpha\beta}E_\alpha E_\beta + \frac{1}{6}\mathbf{C}_{\alpha\beta\gamma}E_\alpha E_\beta E_\gamma,$$
$$\Psi^{(1)} = \Psi_0^{(1)} + \frac{\mu}{2}[(\mathrm{tr}\,\boldsymbol{E})^2 + 2\boldsymbol{E}:\boldsymbol{E}]. \tag{2.9}$$

Since time scale(s) involved in amorphization kinetics are unknown and unavailable from static DFT, a discrete representation is used, and the domain $0 < \zeta < 1$ is ignored in numerical simulations reported later. Recrystallization has not been reported in the literature and is precluded by the model, meaning $\zeta : 0 \to 1$ is irreversible. Following earlier conjecture (Taylor et al., 2011) and analysis (Clayton, 2012), stress-induced amorphization in B_4C at a material point $\boldsymbol{X}$ at time t is prescribed to occur upon attainment of the B-instability criterion:

$$\det[\mathbf{B}(\boldsymbol{X}, t)] \le 0 \Rightarrow \zeta(\boldsymbol{X}, t) \to 1, \tag{2.10}$$

where incremental modulus $\mathbf{B}$ is defined in (A.7) of Appendix A and can be written as a symmetric 6×6 matrix (Wang et al., 1995; Morris and Krenn, 2000; Clayton, 2012). Since $\mathbf{B}$ depends on the local stress-deformation state, amorphization propagates at the elastic wave speed. This transformation model is advantageous because no fitting parameters are introduced. However, in this discrete representation, $\dot{\zeta} \to \infty$ at the instant of amorphization, precluding pragmatic enforcement of the dissipation inequality in (2.6) that requires time differentiability of state variables.

Table 2
Isotropic elastic properties for amorphous phase.

K_1/K_0	ν	Reference
0.96	$\frac{1}{4}$	Ivanshchenko et al. (2009)

3. Numerical method and results

3.1. Finite element method

The constitutive model of Section 2.2 is implemented in a dynamic Lagrangian finite element program. Behavior of a representative microstructure consisting of 50 polyhedral grains (Fig. 1) is studied. The FE mesh, with sufficient refinement near grain boundaries and triple points to resolve local fields, consists of 1.6M hexahedral elements. Software and mesh generation procedures have been discussed in detail elsewhere (Clayton et al., 2012a,b) in the context of other ceramic materials. Faces of the polycrystalline cube are normal to global X, Y, and Z directions. Four initial microstructures are considered with random lattice orientation arrangements labeled 1, 2, 3, and 4, and with $\zeta = 0\ \forall\ \boldsymbol{X}$ at the beginning of each simulation. Lattices 1 and 2 contain mixtures of grains of CCC and polar polytypes; lattices 3 and 4 consist only of randomly oriented crystals of the polar polytype. In dynamic simulations, transformation criterion (2.10) is enacted at an integration point when the minimum eigenvalue of matrix $[\mathbf{B}]$ first becomes nonpositive.

3.2. Shock compression

Boundary conditions establish a planar shock wave that transits across the sample. The edge length of the polycrystalline cube is 40 μm, yielding an average grain size consistent with the real material (Dandekar, 2001). One face of the cube is assigned a uniform pressure boundary condition, ramped from zero to $\bar{p}$ over a small (4 ps) time interval and then held constant for the remainder of the simulation. Lateral boundaries are fixed in the normal direction to maintain a uniaxial strain state, while the face opposite the pressurized face remains free. A number of simulations are conducted with $\bar{p}$ of 10, 15, 20, 30, 40, and 50 GPa, applied to any

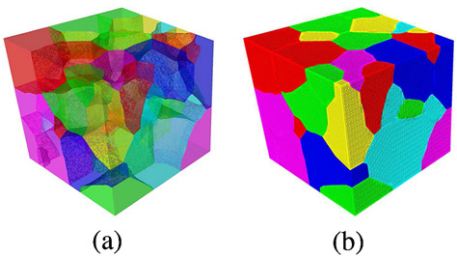

Fig. 1. Synthetic boron carbide polycrystal: (a) grain structure, transparent view and (b) FE mesh.

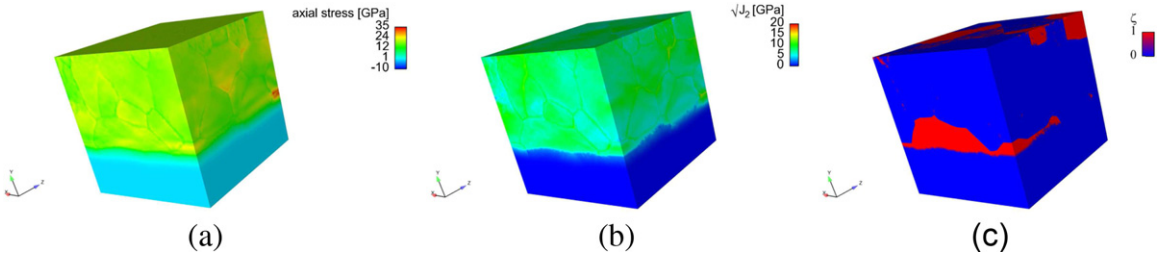

Fig. 2. Shock compression ($\overline{p} = 20$ GPa) of mixture of polytypes at $t = 2$ ns: (a) axial stress, (b) shear stress and (c) order parameter.

of X, Y, or Z faces, with any of lattice arrangements 1–4. Note that the overall stress state is not hydrostatic since $\overline{p}$, the compressive normal component of Cauchy stress, is applied to only one face of the cube.

Representative results for a polycrystal consisting of both polytypes are shown in Fig. 2; analogous results for a polycrystal consisting only of the polar polytype are shown in Fig. 3. In each case, the shock wave is propagating from top to bottom, and has yet to transit the entire sample at 2 ns. The axial component of Cauchy stress, positive in compression, is shown in part (a) of each figure, and can exceed the applied axial pressure $\overline{p}$ by ≈15 GPa. The square root of the second invariant of the deviatoric Cauchy stress, $\sqrt{J_2}$, a measure of the magnitude of local shear stress, has a typical value on the order of 10 GPa and can locally surpass 15 GPa or exceed the theoretical strength ($\approx(1/10)\mathbf{C}_{44}$). Transformation in the mixture of CCC + polar polytypes in Fig. 2(c) tends to involve entire grains (mainly CCC), whereas transformation in the polar polytype in Fig. 3(c) is less pronounced and correlates with areas of concentrated axial stress (Fig. 3(a)) at several grains and grain boundaries. Axial stress versus volume for all simulations are compared with experimental data (Vogler et al., 2004; Zhang et al., 2006) in Fig. 4(a). Hugoniot equations (Clayton, 2010; Thurston, 1974) have been used to estimate "average" volume V in the shocked state and the "average" shock velocity D from simulation data:

$$V = 1\left(\frac{-\rho_0 \overline{v}^2}{P}\right) V_0, \quad D = \frac{P}{\rho_0 \overline{v}}. \tag{3.1}$$

with $V_0 = (40\,\mu\text{m})^3$. Effective particle velocity $\overline{v}$ and shock stress P are estimated from simulation data as

$$\overline{v} \approx \frac{1}{2}\langle v_f \rangle, \quad P \approx \overline{p}, \tag{3.2}$$

with $\langle v_f \rangle$ the arithmetic mean of particle velocities of nodes on the free face of the polycrystalline cube at $t = 5$ ns. Recall that for uniaxial strain in the X_1 direction, axial Cauchy stress (i.e., the Hugoniot "pressure") and axial first Piola–Kirchhoff stress are equal: $\sigma_{11} = J^{-1}F_{1K}P_{1K} = J^{-1}F_{11}P_{11} = P_{11}$, where P_{11} is equivalent in magnitude to P in the Hugoniot relations (Thurston, 1974). The standard Hugoniot relations, with the material in front of the shock at rest, are derived for a homogeneous medium with a planar shock (step discontinuity in stress) in one spatial dimension; Eqs. (3.1) and (3.2) are approximations in the present context because of local heterogeneity, the small but finite thickness of the shock, and stress wave

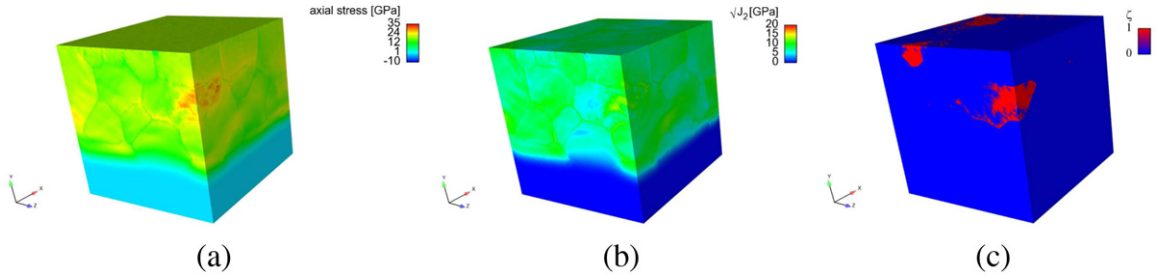

Fig. 3. Shock compression of polar polytype ($\overline{p} = 20$ GPa) at $t = 2$ ns: (a) axial stress, (b) shear stress and (c) order parameter.

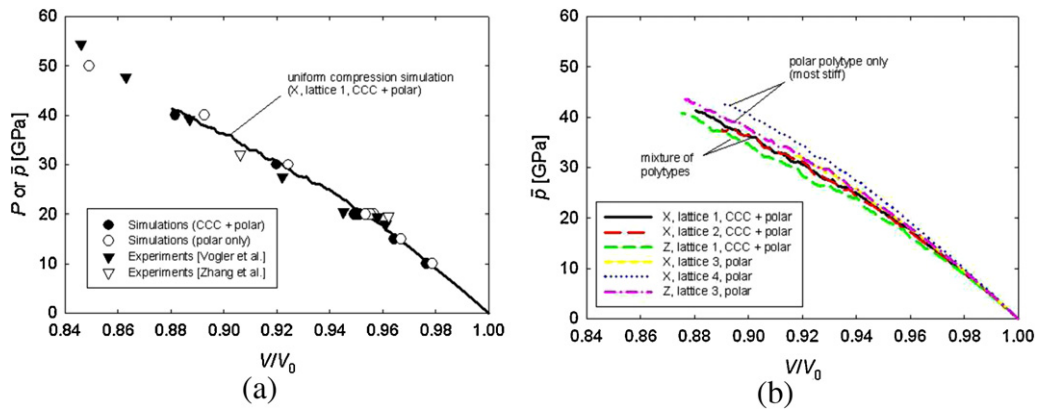

Fig. 4. Axial or shock stress ($\overline{p}$ or P) versus axial compression ratio V/V_0: (a) shock simulations (see Section 3.2), plate impact experiments (Vogler et al., 2004; Zhang et al., 2006) and (b) uniform compression simulations (see Section 3.3).

Table 3
Results summary at $t = 5$ ns, various loading directions and initial microstructures, $P \approx \overline{p} = 20$ GPa shock.

Load dir.	Lattice	Initial polar frac.	$\overline{\zeta}$	$\overline{v}$ (m/s)	D (km/s)	V/V_0
X	1	0.45	0.39	604	13.1	0.954
Y	1	0.45	0.38	622	12.8	0.951
Y	2	0.77	0.24	626	12.7	0.951
Z	1	0.45	0.45	635	12.5	0.949
X	3	1.00	0.09	596	13.3	0.955
Y	3	1.00	0.03	607	13.1	0.954
Y	4	1.00	0.05	586	13.5	0.957
Z	3	1.00	0.06	608	13.1	0.953

interactions with boundaries of the domain. By $t = 5$ ns, the main compressive (shock) wave has fully interacted with the free surface (necessitating the factor of 1/2 in (3.2)), and a nearly steady value of $\overline{v}$ has been reached in each simulation. At that time, some unloading of the sample has occurred upon reflection of the compressive wave at the free surface, but results reveal that further transformation is minimal in unloaded regions of material. This behavior is expected since transformation in B_4C is driven by compressive stress (Clayton, 2012).

Experimental values for Hugoniot stress P and volume ratio $V/V_0 = \rho_0/\rho$ are obtained directly from Vogler et al. (2004) and Zhang et al. (2006). In these experiments, a two-wave structure was observed, whereas in the present simulations, a single-wave structure was observed. In simulations, the length of the domain in the direction of shock propagation was insufficient to permit a fully formed sharp shock with a steady profile prior to arrival at the free surface. It has been shown elsewhere (Clifton, 1971) that even for an isotropic homogeneous nonlinear elastic–plastic material, the propagation distance needed for a steady wave profile to emerge for weak shocks can exceed 0.5–1 mm. Though the first arrival time of the elastic wave could be obtained from simulations, it was not possible to extract a shock velocity D (meaningful for comparison among different cases) directly due to the small but finite rise time of the free surface velocity and heterogeneities induced by grain structure and anisotropy.

Comparison with experiment is reasonable; at each impact pressure, V/V_0 for the polar polytype alone exceeds that for the mixture, demonstrating higher average stiffness of the former (i.e., amorphization tends to decrease axial stiffness). Quantities entering (3.1) are compared for all 20 GPa simulations in Table 3; $\overline{\zeta}$ is the volume fraction of amorphized material in each polycrystal at $t = 5$ ns. Inclusion of the less intrinsically stable CCC polytype correlates with increased transformation and reduced shock velocity. The solid curve in Fig. 4(a) corresponds to a uniform compression simulation as discussed in Section 3.3.

3.3. Uniform compression

Boundary and initial conditions establish an average uniaxial strain state with a nominal strain rate of 10^5/s (Clayton et al., 2012a,b). One face of the cube is assigned a constant velocity boundary condition inducing axial compressive strain. Lateral boundaries are constrained in transverse directions to maintain a uniaxial strain state, while the face opposite the moving face is rigidly fixed. An initial velocity gradient is prescribed consistent with the applied strain rate, so that the material undergoes shockless compression. A number of simulations are conducted with strain applied in any of X, Y, or Z directions, with any of lattice arrangements 1–4. The Courant condition restricts the integration timestep Δt (proportional to the minimum element dimension) and thus the maximum average strain that can be attained at a fixed strain rate $\dot{\epsilon}$. For example, the number of integration cycles (proportional to wall-clock compute time) to achieve a strain $\overline{\epsilon}$ is $n = \overline{\epsilon}/(\dot{\epsilon}\Delta t)$. Therefore, for uniform compression the edge length of the polycrystal cube is set to 1 mm.

Characteristic results for polycrystals of CCC + polar and polar polytype only are shown respectively in Figs. 5 and 6. Local concentrations of axial and shear stress are evident in certain crystals and grain/phase boundaries. Transformation in the polar polytype is visibly restricted to a few small regions (Fig. 6(c)) that correlate with stress concentrations at grain boundaries in Fig. 6(a) and (b). As was the case for shock loading, transformation in the CCC + polar mixture (Fig. 5(c)) involves comparatively large volumes often corresponding to whole grains. Average axial stress $\overline{p}$ (normal force per unit equivalent reference or current area) acting on the moving face of the polycrystal cube is compared for six uniform compression simulations in Fig. 4(b). Undulations correlate with amorphization events. Despite differences in absolute size of specimens, results in Fig. 4(a) and (b) are in reasonable agreement. Again, simulations involving only the polar polytype demonstrate higher average stiffness and less transformation.

3.4. Discussion

Conditions deemed sufficient for onset of amorphization or strength loss are compared in Table 4. For shock simulations (first two rows), $\overline{p}$ is the minimum applied axial pressure at which transformation is observed. For example, for simulations of the polar polytype only, transformation is observed at $\overline{p} = 20$ GPa but not at $\overline{p} = 15$ GPa. Tabulated results for uniform compression are averages over multiple simulations discussed in Section 3.3. Prior analytical results (Clayton, 2012) involve elastostatics and uniform strain among grains. Comparison of these results with those in the first and third rows indicate that stress dynamics and elastic grain interactions promote instability relative to the static and homogeneous case in Clayton (2012). Experimental plate impact data are averages over multiple shots (Vogler et al., 2004; Zhang et al., 2006), with P corresponding to the average HEL, above which a measurable strength loss is evident (Vogler et al., 2004), though amorphization has not been definitively proven to cause such strength reduction. Stress P for ballistic penetration experiments is estimated in Chen et al. (2003), with $\overline{v}$ the projectile velocity. For $\overline{v} \gtrsim 900$ m/s, a marked decrease in ballistic penetration resistance was noted, and the boron carbide target cleaved into numerous fragments containing amorphous zones.

Comparing the present results (first four rows) with others in Table 4, satisfactory agreement is found for simulations involving the polar polytype. Transformation is premature (i.e., $\overline{p}$ is deemed too low) and $\overline{\zeta}$ too high relative to experiment, when the CCC polytype amorphizes upon attainment of intrinsic B-instability criterion (2.10). Thus, the present work suggests that intrinsic instability criterion (2.10) is adequate for initiation of amorphization in the polar polytype, but not the CCC polytype. This result supports the finding from DFT calculations (Yan et al., 2009) that a buckling instability during [0 0 0 1] compression in the polar polytype leads to cross-linking of the B atom of the C–B–C atom chain of the rhombohedral unit cell with one of the icosahedra in the surrounding structural cage, followed by structure collapse and amorphization. Since no B atom exists in the CCC polytype (i.e., its atomic backbone is C–C–C), the same mechanism is not possible in crystals of the CCC polytype in B_4C.

The amorphization model implemented here is simple, with no adjustable parameters, and appears adequate for addressing initiation of transformation. However, some experiments (Chen et al., 2003; Subhash et al., 2008; Yan et al., 2009) report thin bands (several nm) of glassy phase, features that cannot be fully resolved by FE representations of polycrystals with minimum element sizes on the order of tens to hundreds of nm. An alternative numerical technique is needed to resolve such small features. Other nonlinear

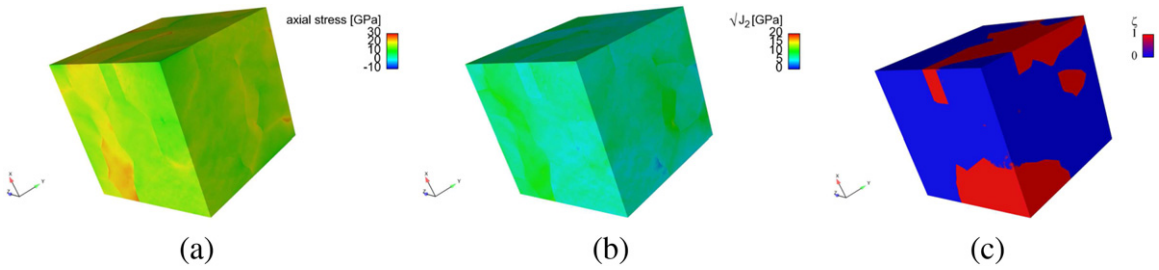

Fig. 5. Uniform compression of mixture of polytypes at $V/V_0 = 0.96$: (a) axial stress, (b) shear stress and (c) order parameter.

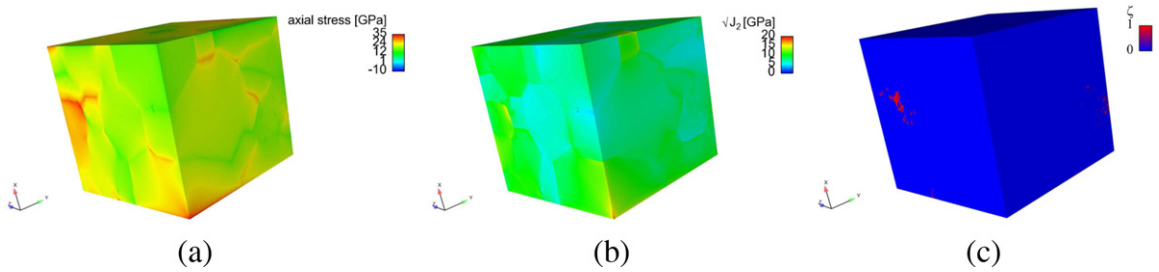

Fig. 6. Uniform compression of polar polytype at $V/V_0 = 0.95$: (a) axial stress, (b) shear stress and (c) order parameter.

models have addressed thermal effects (Clayton, 2009, 2011b) which could be important in shear localization (Grady, 2011) but are not treated here. Plastic slip and twinning have also been analyzed for other ceramics in finite deformation models (Clayton, 2009, 2011b), but (partial) dislocations are thought to be relatively immobile in typical B_4C (Clayton, 2012). Twin boundaries are scarce in conventional boron carbide produced by hot pressing, but are abundant in the less common slip-cast material and affect its stress fields (Sano and Randow, 2011). Fracture, including grain boundary failure and especially intragranular (i.e., cleavage) fracture, inevitably occurs in ballistic impact, and accompanies amorphization in diamond anvil cell (DAC) experiments (Yan et al., 2009). Fracture in boron carbide – which could be modeled using cohesive zone (Clayton, 2005; Clayton et al., 2012a) or continuum damage mechanics (Clayton, 2006; Aslan et al., 2011) techniques – would presumably affect local stress states and amorphization.

The present limited results suggest that for similar values of applied or average compressive stress $\overline{p}$, instability sometimes appears more likely in shock simulations than uniform compression simulations. For example, transformation in the polar polytype occurs at shock stresses between 15 and 20 GPa, but does not occur in uniform compression until 23 GPa (second and fourth rows of Table 4). Statistics from more simulations involving more microstructures are needed to verify this assertion, and the same conclusion cannot be affirmed from the present results for simulations involving a mixture of polytypes. According to the present amorphization model, for the same microstructure, differences in transformation behavior would be due solely to differences in local stress state. In real experiments, entropy and temperature rise during shock loading would tend to exceed that during uniform isentropic compression (Thurston, 1974), and this could promote instability in a way not accounted for by the present simulations that omit thermal effects.

Several other issues warrant further discussion. Results demonstrate that the FE mesh resolution is adequate to resolve transformation zones and stress concentrations, with multiple elements tending to span such regions. For example, contours in Figs. 2, 3, 5 and 6 show that stress concentrations and transformed regions are typically controlled by grain geometry rather than local element sizes and shapes, though in some cases regions of amorphized material approaching the element size were detected. Simulations reported already were conducted with default parameters (Jung, 2010) for linear and quadratic artificial bulk viscosity enabled. Simulations were also explored with viscosity disabled, yielding results that differed little from those shown in Section 3. In shock problems, artificial viscosity is typically used to establish a numerical shock width large enough to be resolved by the grid size (Lew et al., 2002); in the present simulations, the imposed stress wave is ramped and does not localize to a width equal to the local element size. Nevertheless, a more comprehensive study of effects of mesh size/geometry and viscosity may be warranted for general applications of the model. Extension of the amorphization model to a phase field approach (Clayton and Knap, 2011a,b), as mentioned in Section 2.1, could enable regularization of widths of transformation zones and ensure resolution of locally heterogeneous features of the solution that might otherwise depend on mesh density.

Table 4
Sufficient conditions for initiation of structure change and/or strength loss in B_4C.

Simulation or experiment	Polytype(s)	P or $\overline{p}$ (GPa)	$\overline{v}$ (m/s)	V/V_0	Reference
Shock simulation	CCC + polar	15.0	401	0.964	Present work Section 3.2
Shock simulation	Polar	20.0	607	0.954	Present work Section 3.2
Uniform dynamic simulation	CCC + polar	13.1	–	0.969	Present work Section 3.3
Uniform dynamic simulation	Polar	23.0	–	0.948	Present work Section 3.3
Nonlinear elasticity analysis	CCC + polar	18.1	–	0.960	Clayton (2012)
DFT single crystal calculation	Polar	18.9	–	0.930	Yan et al. (2009)
Plate impact experiment	Not reported	16.5	600	0.944	Vogler et al. (2004)
Plate impact experiment	Not reported	19.5	530	0.965	Zhang et al. (2006)
Ballistic penetration experiment	Not reported	23.3	900	–	Chen et al. (2003)

4. Conclusions

A geometrically nonlinear theory for anisotropic elasticity and stress-induced amorphization has been implemented for boron carbide and exercised in dynamic compression simulations of polycrystals. Results for stress–strain behavior, initiation of transformation in the polar polytype associated with loss of intrinsic stability, and strength/stiffness loss compare favorably with atomic theory and experimental observations.

Appendix A. Intrinsic stability

Consider an elastic material with strain energy per unit reference volume $\Psi(\boldsymbol{q})$ undergoing homogeneous deformation. Let $\delta\Psi$ denote an increment in strain energy, and δw a first-order increment in external work at fixed $\boldsymbol{p}$, where $\boldsymbol{q}$ and $\boldsymbol{p}$ are vector representations of generalized coordinates (i.e., deformation) and conjugate force:

$$\delta\Psi = \frac{\partial\Psi}{\partial\boldsymbol{q}}\cdot\delta\boldsymbol{q} + \frac{1}{2}\delta\boldsymbol{q}\cdot\frac{\partial^2\Psi}{\partial\boldsymbol{q}\partial\boldsymbol{q}}\cdot\delta\boldsymbol{q} + \cdots, \quad \delta w = \boldsymbol{p}\cdot\delta\boldsymbol{q}. \tag{A.1}$$

Classical stability requires $\delta\Psi > \delta w$ (Hill, 1975; Parry, 1978). At fixed load (i.e., stationary virtual stress as in (A.1)) with first-order equilibrium constraint $\boldsymbol{p} = \partial\Psi/\partial\,\boldsymbol{q}$ and to second order in $\delta\,\boldsymbol{q}$, "intrinsic" stability criteria emerge:

$$\delta\boldsymbol{q}\cdot\frac{\partial^2\Psi}{\partial\boldsymbol{q}\partial\boldsymbol{q}}\cdot\delta\boldsymbol{q} > 0 \quad (\forall\boldsymbol{q}\neq\boldsymbol{0}) \quad \Leftrightarrow \quad \det\left[\frac{\partial^2\Psi}{\partial\boldsymbol{q}\partial\boldsymbol{q}}\right] > 0. \tag{A.2}$$

Such criteria (which amount to local convexity conditions), while dependent only on the local state, depend non-uniquely on choice $\boldsymbol{q}$ and correlate with classical stability only in certain environments, e.g., load control via $\boldsymbol{p}$. Let $\delta\,\boldsymbol{e} = \boldsymbol{F}^{-\mathrm{T}}\delta\,\boldsymbol{E}\,\boldsymbol{F}^{-1}$, where $\delta\,\boldsymbol{E}$ is an increment in Green strain. Incremental external work per unit reference volume is

$$\delta w = \boldsymbol{S} : \delta\boldsymbol{E} = \boldsymbol{P} : \delta\boldsymbol{F} = J\boldsymbol{\sigma} : \delta\boldsymbol{e}. \tag{A.3}$$

Born's mechanical stability criterion (Born, 1940) involves the choices and $\boldsymbol{q}\to\boldsymbol{E}$ and $\boldsymbol{p}\to\boldsymbol{S} = \partial\Psi/\partial\,\boldsymbol{E}$, with spatial ($\mathbf{c}$) and referential ($\mathbf{C}$) tangent elastic moduli related by $\mathbf{c}_{ijkl} = J^{-1}F_{iI}F_{jJ}F_{kK}F_{lL}\mathbf{C}_{IJKL}$:

$$\begin{aligned}\delta\boldsymbol{S} : \delta\boldsymbol{E} &= \delta\boldsymbol{E} : \frac{\partial^2\Psi}{\partial\boldsymbol{E}\partial\boldsymbol{E}} : \delta\boldsymbol{E} = \delta\boldsymbol{E} : \mathbf{C} : \delta\boldsymbol{E}\\ &= J\delta\boldsymbol{e} : \mathbf{c} : \delta\boldsymbol{e} > 0 \Leftrightarrow \det[\mathbf{C}] > 0 \Leftrightarrow \det[\mathbf{c}] > 0.\end{aligned} \tag{A.4}$$

For intrinsic stability consistent with classical stability under all-around dead loading (Hill, 1975; Ogden, 1984), $\boldsymbol{q}\to\boldsymbol{F}$ and $\boldsymbol{p}\to\boldsymbol{P} = \partial\Psi/\partial\,\boldsymbol{F}$:

$$\begin{aligned}&\delta\boldsymbol{P} : \delta\boldsymbol{F} = \delta\boldsymbol{F} : \frac{\partial^2\Psi}{\partial\boldsymbol{F}\partial\boldsymbol{F}} : \delta\boldsymbol{F} = \delta\boldsymbol{F} : \mathbf{A} : \delta\boldsymbol{F} > 0 \Leftrightarrow \det[\mathbf{A}] > 0;\\ &\mathbf{A}_{iJkL} = F_{iI}F_{kK}\mathbf{C}_{IJKL} + S_{JL}\delta_{ik}.\end{aligned} \tag{A.5}$$

For intrinsic stability consistent with classical stability under controlled Cauchy stress (Wang et al., 1995; Morris and Krenn, 2000), $\boldsymbol{p}\to\boldsymbol{\sigma}$ and $\boldsymbol{q}\to\boldsymbol{e}$:

$$\delta\boldsymbol{\sigma} : \delta\boldsymbol{e} = \left[\frac{\partial\boldsymbol{\sigma}}{\partial\mathbf{E}} : \delta\boldsymbol{E}\right] : \delta\boldsymbol{e} = \delta\boldsymbol{e} : \mathbf{B} : \delta\boldsymbol{e} > 0 \Leftrightarrow \det[\mathbf{B}] > 0; \tag{A.6}$$

$$\mathbf{B}_{ijkl} = \mathbf{c}_{ijkl} + \frac{1}{2}(\sigma_{ik}\delta_{jl} + \sigma_{il}\delta_{jk} + \sigma_{jl}\delta_{ik} + \sigma_{jk}\delta_{il} - \sigma_{ij}\delta_{kl} - \sigma_{kl}\delta_{ij}). \tag{A.7}$$

Incremental spatial modulus $\mathbf{B}$ was derived 45 years ago by Wallace (1967) but has only been used more recently in general stability criteria. The first two equalities in (A.6) strictly apply only when $\boldsymbol{F}$ is symmetric, but the inequalities apply regardless since $\mathbf{B}$ is rotationally invariant. In the former case, it can be proven that definition (A.7) is exact when $\delta^2\,\boldsymbol{E}\to\boldsymbol{0}$ (Clayton, 2012). This criterion agrees exactly with that for classical stability under hydrostatic loading (Milstein and Hill, 1979). Correlations are likely, but not always necessary, among failure of intrinsic stability criteria in perfect crystals and the onset of various structural changes, e.g., melting, cavitation, slip, twinning, or solid–solid phase transitions (Born, 1940; Hill, 1975; Parry, 1980b; Wang et al., 1995; Morris and Krenn, 2000).

References

Aslan, O., Codero, N., Gaubert, A., Forest, S., 2011. Micromorphic approach to single crystal plasticity and damage. International Journal of Engineering Science 49, 1311–1325.

Born, M., 1940. On the stability of crystal lattices. I. Mathematical Proceedings of the Cambridge Philosophical Society 36, 160–172.

Chen, M., McCauley, J., Hemker, K., 2003. Shock-induced localized amorphization in boron carbide. Science 299, 1563–1566.

Clayton, J., Bliss, K. Analysis of intrinsic stability criteria for isotropic third-order green elastic and compressible neo-Hookean solids, in progress, unpublished.

Clayton, J., Knap, J., 2011a. A phase field model of deformation twinning: nonlinear theory and numerical simulations. Physica D 240, 841–858.

Clayton, J., Knap, J., 2011b. Phase field modeling of twinning in indentation of transparent crystals. Modelling and Simulation in Materials Science and Engineering 19, 085005.

Clayton, J., Kraft, R., Leavy, R., 2012a. Mesoscale modeling of nonlinear elasticity and fracture in ceramic polycrystals under dynamic shear and compression. International Journal of Solids and Structures 49, 2686–2702.

Clayton, J., Leavy, R., Kraft, R., 2012b. Dynamic compressibility, shear strength, and fracture behavior of ceramic microstructures predicted from mesoscale models. In: Elert, M., Buttler, W., Furnish, M. (Eds.), Shock Compression of Condensed Matter, vol. 1426. AIP Conference Proceedings, pp. 1039–1044.

Clayton, J., 2005. Dynamic plasticity and fracture in high density polycrystals: constitutive modeling and numerical simulation. Journal of the Mechanics and Physics of Solids 53, 261–301.

Clayton, J., 2006. Continuum multiscale modeling of finite deformation plasticity and anisotropic damage in polycrystals. Theoretical and Applied Fracture Mechanics 45, 163–185.

Clayton, J., 2009. A continuum description of nonlinear elasticity, slip, and twinning, with application to sapphire. Proceedings of the Royal Society A 465, 307–334.

Clayton, J., 2010. Modeling nonlinear electromechanical behavior of shocked silicon carbide. Journal of Applied Physics 107, 013520.

Clayton, J., 2011a. Nonlinear Mechanics of Crystals. Springer, Dordrecht.

Clayton, J., 2011b. A nonlinear thermomechanical model of spinel ceramics applied to aluminum oxynitride (AlON). Journal of Applied Mechanics 78, 011013.

Clayton, J., 2012. Towards a nonlinear elastic representation of finite compression and instability of boron carbide ceramic. Philosophical Magazine 92, 2860–2893.

Clifton, R., 1971. On the analysis of elastic visco-plastic waves of finite uniaxial strain. In: Burke, J.J., Weiss, V. (Eds.), Shock Waves and the Mechanical Properties of Solids. Syracuse University Press, New York, pp. 73–116.

Dandekar, D., 2001. Shock response of boron carbide. Tech. Rep. ARL-TR-2456, US Army Research Laboratory, Aberdeen Proving Ground, MD.

Dodd, S., Saunders, G., James, B., 2002. Temperature and pressure dependences of the elastic properties of ceramic boron carbide (B_4C). Journal of Materials Science 37, 2731–2736.

Fanchini, G., McCauley, J., Chhowalla, M., 2006. Behavior of disordered boron carbide under stress. Physical Review Letters 97, 035502.

Grady, D., 2011. Adiabatic shear failure in brittle solids. International Journal of Impact Engineering 38, 661–667.

Gregoryanz, E., Hemley, R., Mao, H., Gillet, P., 2000. High-pressure elasticity of α-quartz: instability and ferroelastic transition. Physical Review Letters 84, 3117–3120.

Hill, R., 1975. On the elasticity and stability of perfect crystals at finite strain. Mathematical Proceedings of the Cambridge Philosophical Society 77, 225–240.

Ivanshchenko, V., Shevchenko, V., Turchi, P., 2009. First principles study of the atomic and electronic structures of crystalline and amorphous B_4C. Physical Review B 80, 235208.

Jung, J., 2010. Presto 4.16 user's guide. Tech. Rep. SAND2010-3112, Sandia National Laboratories, Albuquerque, NM.

Lee, S., Bylander, D., Kleinman, L., 1992. Elastic moduli of B_{12} and its compounds. Physical Review B 45, 3245–3247.

Lew, A., Radovitzky, R., Ortiz, M., 2002. An artificial-viscosity method for the Lagrangian analysis of shocks in solids with strength on unstructured, arbitrary-order tetrahedral meshes. Journal of Computer-Aided Materials Design 8, 213–231.

McClellan, K., Chu, F., Roper, J., Shindo, I., 2001. Room temperature single crystal elastic constants of boron carbide. Journal of Materials Science 36, 3403–3407.

Milstein, F., Hill, R., 1979. Theoretical properties of cubic crystals at arbitrary pressure – III. Stability. Journal of the Mechanics and Physics of Solids 27, 255–279.

Morris, J., Krenn, C., 2000. The internal stability of an elastic solid. Philosophical Magazine A 80, 2827–2840.

Ogden, R., 1984. Non-Linear Elastic Deformations. Ellis-Horwood, Chichester.

Parry, G., 1978. On the relative strengths of intrinsic stability criteria. Quarterly Journal of Mechanics and Applied Mathematics 31, 1–7.

Parry, G., 1980a. On the relative strengths of stability criteria in anisotropic materials. Mechanics Research Communications 7, 93–98.
Parry, G., 1980b. On structural phase transitions in perfect crystals. Mechanics Research Communications 8, 341–348.
Pineda, E., 2006. Theoretical approach to Poisson ratio behavior during structural changes in metallic glasses. Physical Review B 73, 104109.
Sano, T., Randow, C., 2011. The effect of twins on the mechanical behavior of boron carbide. Metallurgical and Materials Transactions A 42, 570–574.
Subhash, G., Maiti, S., Geubelle, P., Ghosh, D., 2008. Recent advances in dynamic indentation fracture, impact damage and fragmentation of ceramics. Journal of the American Ceramic Society 91, 2777–2791.
Taylor, D., Wright, T., McCauley, J., 2011. First principles calculation of stress induced amorphization in armor ceramics. Tech. Rep. ARL-MR-0779, US Army Research Laboratory, Aberdeen Proving Ground, MD.
Thurston, R., 1974. Waves in Solids. In: Truesdell, C. (Ed.), Handbuch der Physik VIA/4. Springer-Verlag, Berlin, pp. 287–291.
Vogler, T., Reinhart, W., Chhabildas, L., 2004. Dynamic behavior of boron carbide. Journal of Applied Physics 95, 4173–4183.
Wallace, D., 1967. Thermoelasticity of stressed materials and comparison of various elastic constants. Physical Review 162, 776–789.
Wang, J., Li, J., Yip, S., Phillpot, S., Wolf, D., 1995. Mechanical instabilities of homogeneous crystals. Physical Review B 52, 627–635.
Yan, X., Tang, Z., Zhang, L., Guo, J., Jin, C., Zhang, Y., Goto, T., McCauley, J., Chen, M., 2009. Depressurization amorphization of single-crystal boron carbide. Physical Review Letters 102, 075505.
Zhang, Y., Mashimo, T., Uemura, Y., Uchino, M., Kodama, M., Shibata, K., Fukuoka, K., Kikuchi, M., Kobayashi, T., Sekine, T., 2006. Shock compression behaviors of boron carbide (B_4C). Journal of Applied Physics 100, 113536.

NO. OF COPIES	ORGANIZATION
1 (PDF)	DEFENSE TECHNICAL INFORMATION CTR DTIC OCA
1 (PDF)	DIRECTOR US ARMY RESEARCH LAB RDRL CIO LL
1 (PDF)	GOVT PRINTG OFC A MALHOTRA

ABERDEEN PROVING GROUND

NO. OF COPIES	ORGANIZATION
38 (PDF)	DIR USARL
	RDRL CIH C
	P CHUNG
	J KNAP
	RDRL WM
	B FORCH
	J MCCAULEY
	P PLOSTINS
	RDRL WML B
	I BATYREV
	B RICE
	D TAYLOR
	N WEINGARTEN
	RDRL WML H
	B SCHUSTER
	RDRL WMM
	J BEATTY
	RDRL WMM B
	G GAZONAS
	C RANDOW
	T SANO
	RDRL WMM E
	T BEAUDET
	J DUNN
	J LASALVIA
	J SINGH
	J SWAB
	RDRL WMP
	S SCHOENFELD
	RDRL WMP B
	C HOPPEL
	D POWELL
	S SATAPATHY
	M SCHEIDLER
	T WEERISOORIYA
	RDRL WMP C
	R BECKER
	S BILYK
	T BJERKE
	D CASEM
	J CLAYTON
	D DANDEKAR
	M GREENFIELD
	R LEAVY
	M RAFTENBERG
	S SEGLETES
	C WILLIAMS
	RDRL WMP D
	R DONEY
	RDRL WMP E
	S BARTUS

INTENTIONALLY LEFT BLANK.